scientific reports

OPEN   The role of structural parameters on efficiency and transparency of semi-transparent non-fullerene organic solar cell

Elmira Annabi Milani[1,2], Mina Piralaee[2], Sohrab Ahmadi[1] & Asghar Asgari[1,2,3]✉

Semitransparent organic solar cells have become attractive recently because of their photon harvesting in the near-infrared and ultraviolet range and passing in the visible light region. Semitransparent organic solar cells with ITO/ZnO/PBDB-T:ITIC/MoO3/Ag/MoO3 structure have been studied in this work and the effects of PBDB-T:ITIC active layer thicknesses and the transparent top electrode, MoO_3/Ag/MoO_3, thickness on the solar cell performance such as I-V characteristics, the power conversion efficiency, the average visible transmittance, and the color coordinates in the CIE color space are investigated. The drift–diffusion model, including the density of exactions, and their displacement is used to model the devices. The model is examined with experimentally reported devices, where there is a very good agreement between them, then is applied to the new structures. The obtained results show that the average visible transmittance of more than 45% is achievable for these structures with reasonable power conversion efficiency.

Solar energy, besides fusion, has the greatest potential to meet global future needs as one of the main sources of renewable energy. Therefore, harnessing the power of the sun with photovoltaic technologies seems to be the only practical response on a large scale to the energy challenge. On the other hand, organic solar cells (OSCs) have many advantages over conventional inorganic cells such as low cost, light-weight, and intrinsic flexibility [1], and can be easily produced in thin rolls, any desired color, and can bend and flex in a specific structure or even inside clothing. Integrating flexible OSCs inside clothing, called carry-on photovoltaics, provides a much larger area for integrated photovoltaics than the ever-shrinking portable devices themselves[2].

Another important property of OSCs is their flexibility at the wavelength range of absorption spectra because the optical band gap of organic semiconductors can be simply tuned. So, OSCs can adsorb the infrared (IR), and ultraviolet (UV) regions and passes through the visible light. Therefore, those can be used as a window. Generally, the main purpose of windows is to provide natural light with a clear vision, which has been achieved by developing a semitransparent organic solar cells (ST-OSC) technology that selectively harvests near-infrared (NIR) and UV light and passes them in the visible light region. The power-production from UV and NIR photons alone leads to a theoretical single-junction efficiency of 21% in transparent structures. To have higher efficiency, ST-OSC requires a high-quality active layer because they are more sensitive to shunt-leakage[3,4]. Recently, it has been reported that the ST-OSC with 10 nm Ag achieved a PCE of 12.91% which could be in the range of the best-reported performance of ST-OSC[5].

The thickness of the active layer is important for SC-OSC performance, besides its transparency. The thickness of organic active layers in OSC-based photovoltaic technology is about one hundred nanometers which are sufficient to capture photons. Also, the thickness of each layer is of importance because the wavelength-specific interference pattern of the optical field will vary depending on the exact device architecture[6].

Despite the many advantages, OSCs are still not efficient enough to compete with conventional energy sources, and their large-scale production process for industrial commercialization must be facilitated[7].

Numerous studies have been conducted to improve the power conversion efficiency (PCE), such as the acceptance of solvent additives, applying different active layers, the use of thermal or solvent annealing processes, and the use of triple strategy and reverse structure cells that will be seen in future developments probably[8].

[1]Faculty of Physics, University of Tabriz, Tabriz 51665-163, Iran. [2]Photonics Devices Research Group, Research Institute of Applied Physics and Astronomy, University of Tabriz, Tabriz 51665-163, Iran. [3]School of Electrical, Electronic, and Computer Engineering, University of Western Australia, Crawley, WA 6009, Australia. ✉email: asgari@tabrizu.ac.ir
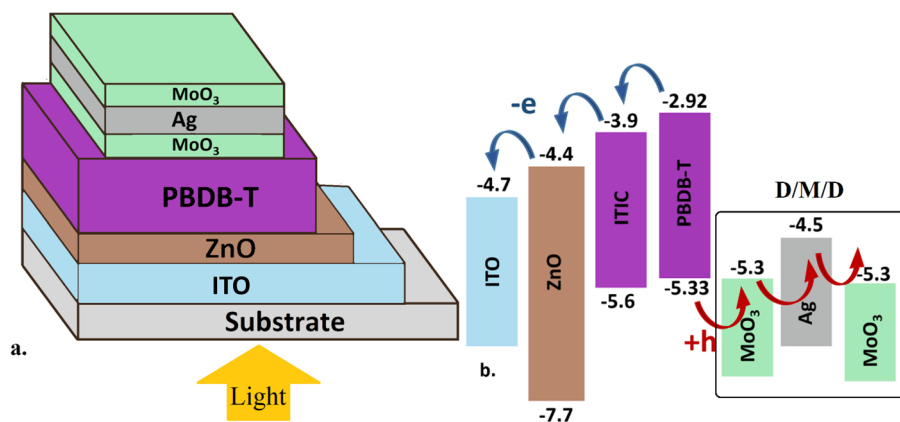
Figure 1. (**a**) Schematic structure, (**b**) The energy level diagram of the materials used in the ST-OSC studied structure [31].

To fabricate an ST-OSC, the light absorption inside the active layer must be precisely adjusted to transmit sufficient visible light[9,10]. In addition, both electrodes must be transparent. Although in OSC, the amount of inter-facial recombination is affected significantly by the electrode choice, a broader range of materials and deposition techniques can be considered for transparent electrodes because the surface recombination at the active layer interfaces is not a dominant recombination mechanism in these systems, therefore, the limitations due to high series resistance decrease[11]. There are several ways to fabricate transparent electrodes. Carbon nanotubes are suitable candidates because they are both cheaper to produce and have good mechanical flexibility[12]. Another carbon-based solution, graphene, has also been studied and used as the top and bottom electrode in semi-transparent organic solar cells. However, these electrodes have low conductivity and require additional chemical doping[13,14]. Single or multiple pairs of one-dimensional photonic crystals can also be used as the top electrode to achieve an efficiency of about 5–6% in the average visible transmittance (AVT) of 25%, of which deposition of multiple layers of metal oxide (MoO_3 or WO_3) /LiF pairs is necessary[15,16]. Depending on applications such as sunglasses, building windows, tinted car windows, etc.…, AVT can vary from about 100% to 25% [17]. Another possible choice for the upper electrode is the dielectric/metal/dielectric (D/M/D) structure. Due to its relatively simple construction and simple fabrication technique, it is more useful in comparison to the alternative approaches such as photonic crystals or graphene-based electrodes[18]. These electrodes have been used in this study.

Also, a significant issue in achieving high efficiency in a device is engineering to select the appropriate material to use as the active layer of OSC. Recently, non-fullerene small molecule acceptors have appeared in OSCs as a viable alternative to conventional fullerene acceptors as electron collectors[19–23]. The reason for the superior performance of non-fullerene OSCs is the enhanced optical and electronic properties of non-fullerene receptors, as a result of easy adjustment of molecular energy levels[24,25], superior optical absorption properties[26], the easy synthesis of these materials and therefore low manufacturing costs. As a result of the mentioned features, non-fullerene acceptors compared to fullerene acceptors[27,28] have accelerated the improvement of OSC's performance over the past few years. For example, the non-fullerene acceptor ITIC has shown particularly promising results. This novel small molecule material has a high lying LUMO level (-3.78 eV), which leads to high open-circuit voltage (V_{oc})[29]. and when coupled with a new polymer (PBDB-T), the efficiency is recorded to be more than 11%[30].

The carrier's recombination is a major loss mechanism in OSCs that controls their performance. Considering the recent progress in improving the donor and acceptor materials used in OSCs, a detailed study of the optical properties of the device is very important to further understand dominant recombination mechanisms in OSCs. In the study of such systems, generally, just the contribution of bimolecular recombination and in some cases bulk-trap-assisted recombination is considered, therefore, it is more desirable to include the interfacial recombination mechanisms in these types of structures[23].

In this work, we have theoretically studied and modeled the role of using PBDB-T:ITIC non-fullerene material in ST-OSCs architecture and considered the effects of the active layer and D/M/D layer thickness on the performance parameters and also AVT of the device.

Method and material

The studied structure used for this study, schematically shown in Fig. 1, is the same as the device reported in Ref [31] with ITO/ZnO/PBDB-T:ITIC/MoO_3/Ag/MoO_3 structure, but with a different active layer and D/M/D layers' thickness. Where MoO_3/Ag/MoO_3 acts as the transparent top electrode, the inner MoO_3 layer also acts as the hole transport layer. Sol–gel processed ZnO layer is used as the electron transport layer and ITO is the transparent bottom electrode.

The combination of PBDB-T and ITIC in the opaque blend structure has previously shown good photovoltaic performance with more than 11% PCE[29]. When it was employed in the semitransparent (ST) structure (Fig. 1a), PCE > 7% was achieved at 25% AVT.

To calculate the device's performance parameters such as the short-circuit current (J_{sc}), the open-circuit voltage (V_{oc}), the fill-factor (FF), and the power conversion efficiency (PCE), we used the drift–diffusion model

including the density of excitons and their displacement. To calculate the density of electrons, holes, and excitons in the interface regions, we have used the theoretical model based on Koster et al.[32]. The model contains the drift–diffusion of charge carriers and the effect of space charge on the electric field in the device. Recombination is described as a bimolecular process, with the rate given by Langevin[33].

One of the easiest and most efficient methods for calculating the reflection, transmission, and absorption spectra in optical multilayers is the Transfer-Matrix Method, TMM[34]. we have used TMM to model the whole device transparency, $T(\lambda)$, knowing the transmittance of each layer[6].

The transparency properties of the device are determined by the transmittance characteristics in the visible light wavelength range (370–740 nm), called the average visible transmittance (AVT), taking into account the photopic response of the human eye (λ). The AVT value is calculated as follows[35,36]:

$$AVT = \frac{\int_{370\,nm}^{780\,nm} S_{AM1.5G}\, T(\lambda)\, V(\lambda)\, d\lambda}{\int_{370\,nm}^{780\,nm} S_{AM1.5G}\, V(\lambda)\, d\lambda},$$ (1)

where $S_{AM1.5}(\lambda)$ is the photon flux under AM 1.5G illumination and $V(\lambda)$ is the photopic response of the human eyes. AVT value of 25% is an acceptable criterion for window applications where it depends on the devices' working circumstances[37]. As the window transparency depends on the human eye's response, the color coordinates (x, y) in the CIE 1931 chromaticity diagram will be another important characteristic of the semi-transparent solar cells. CIE is the most significant system developed by the Commission Internationale de L'Eclairage (CIE, the International Commission on Illumination) to quantify and characterize colors and human perception of color. The color coordinates are calculated using Eq. (2)[9]:

$$x = \frac{X_1}{\sum\limits_{i=1}^{3} X_i}, \ y = \frac{X_2}{\sum\limits_{i=1}^{3} X_i},$$ (2)

where $X_i = \int_{370\,nm}^{780\,nm} S_{AM1.5G}^{D65}\, T(\lambda)\, \overline{x}_i(\lambda)\, d\lambda$, and $S_{AM1.5G}^{D65}$ is the CIE standard D65 illuminant spectrum, and the terms $\overline{x}_i(\lambda)$ are color-matching functions defined by the CIE protocol (X + Y + Z = 1).

Results and discussion

This work has studied ITO/ZnO/PBDB-T:ITIC/MoO₃/Ag/MoO₃ structure with different active layer thicknesses and various D/M/D thicknesses. The thicknesses of active layers are 53, 59, 72, 91, 100, 114, 143 nm, and DMD (Top contact) thickness are 10 (nm)/d_m/30(nm) with d_m: 4, 6, 8, 10, 12, 14, 16 nm. We first examined our model's accuracy in comparison with experimental data reported for the device in Ref.[38], in which the D/M/D thickness is fixed to (6 nm/10 nm/40 nm), and active layer thickness varies from 53 to 143 nm. As shown in Figs. 2, 3, 4, the obtained results are in very good agreement with the experimental results. The characteristics parameters are listed in Table 1. To model the ST-OSC's performances, one has to know the absorption coefficient of the devices with the structures including different layers, especially for different thicknesses of active layers. For this purpose, we calculated the absorption coefficient as a function of the active layer thickness and fitted it to the absorption coefficient reported experimentally. The fitted relation is presented in Eq. (3), which can predict the absorption coefficient for any thickness of the active layer.

$$\alpha_L \approx \left(\frac{(-37.12 + 100\lambda) + \left(0.97 - 3e6\lambda + 2.85e12\lambda^2\right)L}{(-37.12 + 100\lambda) + \left(0.97 - 3e6\lambda + 2.85e12\lambda^2\right)L_0} \right) \times \alpha_{L_0};$$ (3)

where λ is the wavelength, and L is the active layer thicknesses. Knowing the absorption coefficient, α_{L_0}, for an active layer thickness, L_0, which is reported experimentally, one can find the absorption coefficient for any other thicknesses at different wavelengths.

Figure 2 shows the J-V curve of the devices with structure of ITO/ ZnO/ PBDB-T: ITIC/ MoO3/ Ag/ MoO3, with fixed thickness of D/M/D in 6 nm/10 nm/49 nm, and PBDB-T: ITIC active layer thickness is: a) 53, b) 59, c) 72, d) 91, e) 100, f) 114, g) 143 nm. It is clear from the figures, that there is very good agreement between our model and experimental results. This figure indicates that all devices have the same V_{oc}, which is close to 0.85 V. This value is ~ 0.2 V higher than devices containing traditional fullerene acceptors, due to the high LUMO of non-fullerene acceptors[29]. This is a major factor that helps improve this material system's photovoltaic performance. As the active layer thickness was increasing, the J_{sc} also is increasing.
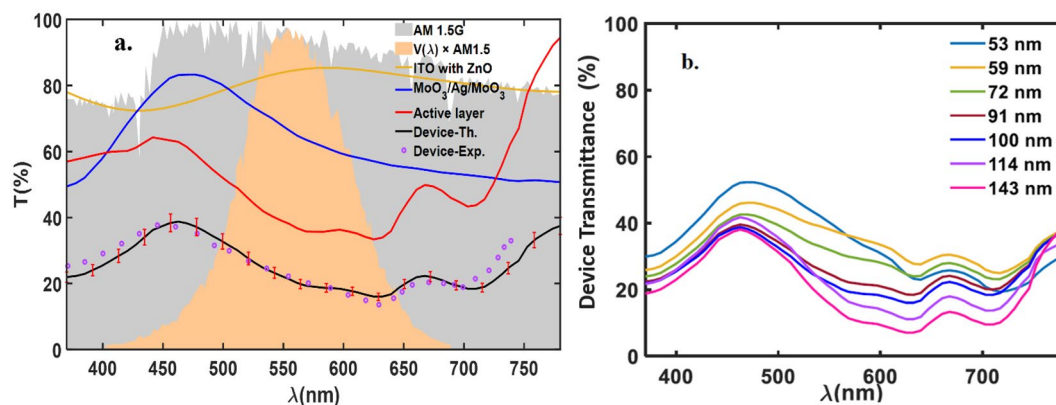
The transmittance spectrum of the ST-OSC for different active layer thicknesses is calculated and compared with those experimental data. As an example, the transmittance spectrum of the ST-OSC with an active layer of 100 nm is presented in Fig. 3a. The figure shows the experimental transmittance for whole devices, besides, the calculated transmittance of the: MoO3/Ag/MoO3 anode, ITO and ZnO compact layer, the active layer, and the whole device. Moreover, for a better understanding of the device's semi-transparency, AM1.5 spectral irradiance, $S_{AM1.5}(\lambda)$, and $S_{AM1.5}(\lambda) * V(\lambda)$ are demonstrated. It can be seen that there is a good agreement between the obtained transparency for the device and the experimental data. Also, the error bar is included which shows the model's accuracy. In the wavelengths of FWHM of $S_{AM1.5}(\lambda) * V(\lambda)$, the ITO and ZnO compact layer has more than 85% transparency, and the MoO3/Ag/MoO3 anode transparency is about 60% to 75%, and active layer transparency is about 35% ~ 50%.

In Fig. 3b, the calculated transmittance of the ST-OSC for different active layers thickness is presented. As shown in the figure, the transmittance of the ST-OSC with thin active layers thickness (53–72 nm) is higher than 25% at all wavelengths of FWHM of $S_{AM1.5}(\lambda) * V(\lambda)$, which makes it much suitable for widow application.
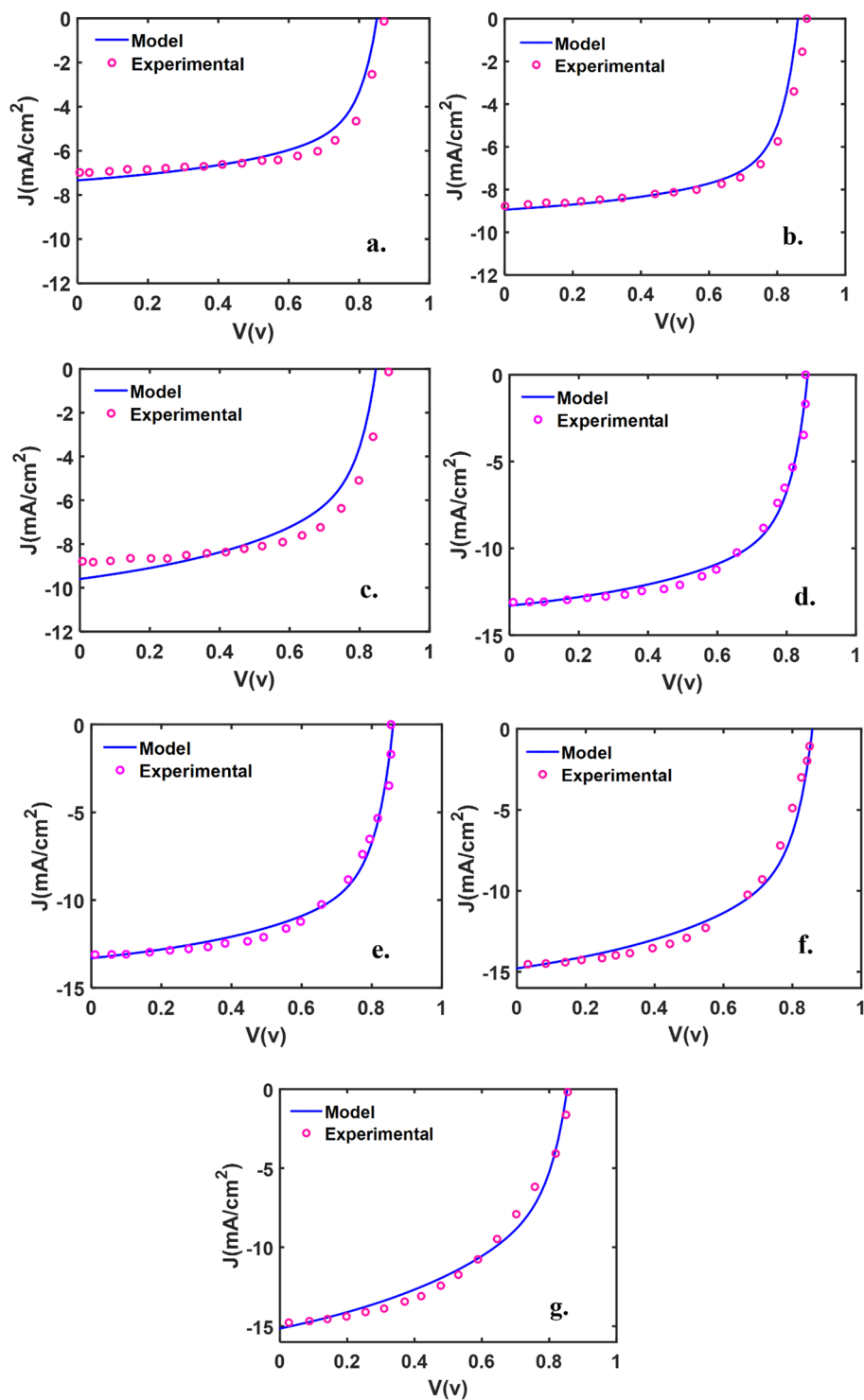
Figure 2. The J-V characteristics of the device with the structure of ITO/ ZnO/ PBDB-T: ITIC/ MoO3/ Ag/ MoO3, with D/M/D thickness of 6 nm/10 nm/40 nm, and PBDB-T: ITIC active layer thickness is: (**a**) 53, (**b**) 59, (**c**) 72, (**d**) 91, (**e**) 100, (**f**) 114, (**g**) 143 nm.

By exceeding the increment of the active layer thickness, the transmittance of the ST-OSC decreases, whereas, for a longer wavelength, it decreases to less than 25%. However, the AVT of the solar cells in the visible region (370–740 nm) of the devices with active layer thickness thinner than 100 nm is higher than 25% and still suitable for widow application.

Figure 3. (**a**) The calculated transmittance spectrum of the active layer (100 nm), $MoO_3/Ag/MoO_3$, ITO with ZnO compact layer, the whole device, both theoretical (solid line) and experimental (dotted), AM1.5 spectral irradiance, and $V(\lambda).S_{AM1.5}(\lambda)$. (**b**) The calculated transmittance spectrum of the devices for different active layer thicknesses.
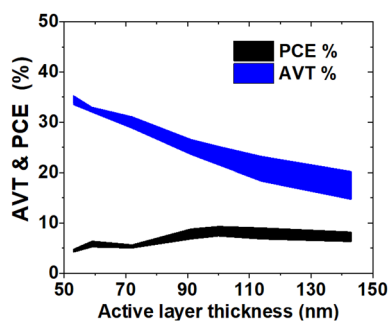
Figure 4. The PCE and AVT, as a function of active layer thickness. The filled area shows the difference between the experimental and theoretical data.

Parameter	value
N_A (1/cm^3)	5e25
N_D (1/cm^3)	5e25
N_c (1/cm^3)	8e27
N_v (1/cm^3)	8e27
Electron Lifetime(s)	8.5e-6
Hole Lifetime(s)	7.5e-6
$V_{\text{built-in}}$ (V)	1.14
Mobility (cm^2/V.s)	variable

Table 1. Parameters used in the calculation for the device modeling.

In Table. 2, we compared the parameters of the solar cell such as short-circuit current, open-circuit voltage, FF, PCE, AVT, and resistances of the modeled devices with experimental data[31]. In Table.2, **Th.** represents the calculated data, and **Exp.** represents the experimental data reported by [31].

As expected and depicted in Table 2 and Fig. 4, with increasing the thickness of the active layer, the photo-absorption increases, and consequently PCE increases. Then, PCE has been decreasing as FF decreases because of the explained recombination effects. FF almost declined with increasing active layer thickness, which is associated with the decrease in shunt resistance values[39,40]. Although the J_{sc} is highest for the active layer with a thickness of 143 nm, the FF is low and is 49.6%. The optimum PCE is obtained at the active layer thickness of 100 nm with a maximum PCE value of 9.32%.

Unlike the PCE, the AVT decreases with increasing active layer thickness. As shown in Fig. 4, and Table 2, for the purposed structures, the devices with PCE of more than 5% and AVT of more than 32% are achievable. The

Thickness (nm)	J_{sc} (mA/cm²)		V_{oc} (V)		FF (%)		PCE (%)		AVT(%)		R_s (Ω.cm²)		R_{sh} (Ω.cm²)	
	Th	Exp	Th	Exp	Th	Exp	Th	Exp	Th	Exp	Th	Exp	Th	Exp
53	7.33	6.85	0.853	0.884	59.50	66.5	4.79	4.2	33.5	35.3	12.07	13.6	2087	1868
59	8.94	8.41	0.86	0.89	63.95	66.9	6.4	5.2	32.0	33	9.91	15.4	1652	1578
72	9.5	8.75	0.863	0.897	54.75	63.2	5.66	5.01	28.8	31.1	11.82	14	1670	1446
91	13.30	12.62	0.867	0.87	59.57	59.4	8.81	6.8	23.6	26.6	12.92	12.9	1174	1176.3
100	14.28	13.8	0.867	0.886	59	59	9.32	7.4	21.5	25.2	11.73	11.9	990.6	977.4
114	14.76	15.08	0.854	0.87	55.51	51.5	9.02	6.8	18.3	23.2	16.51	15.4	503.2	542.4
143	15.14	13.82	0.854	0.89	49.41	49.2	8.21	6.3	14.7	20.2	19.42	19.5	584.7	582.4

Table 2. The calculated characteristic parameters of the ITO/ZnO/PBDB-T:ITIC/MoO₃/Ag/MoO₃ structures with a variation of PBDB-T:ITIC active layer thickness in comparison to experimental data [31]. MoO₃/Ag/MoO₃ thickness is fixed to (6 nm/10/nm/40 nm).
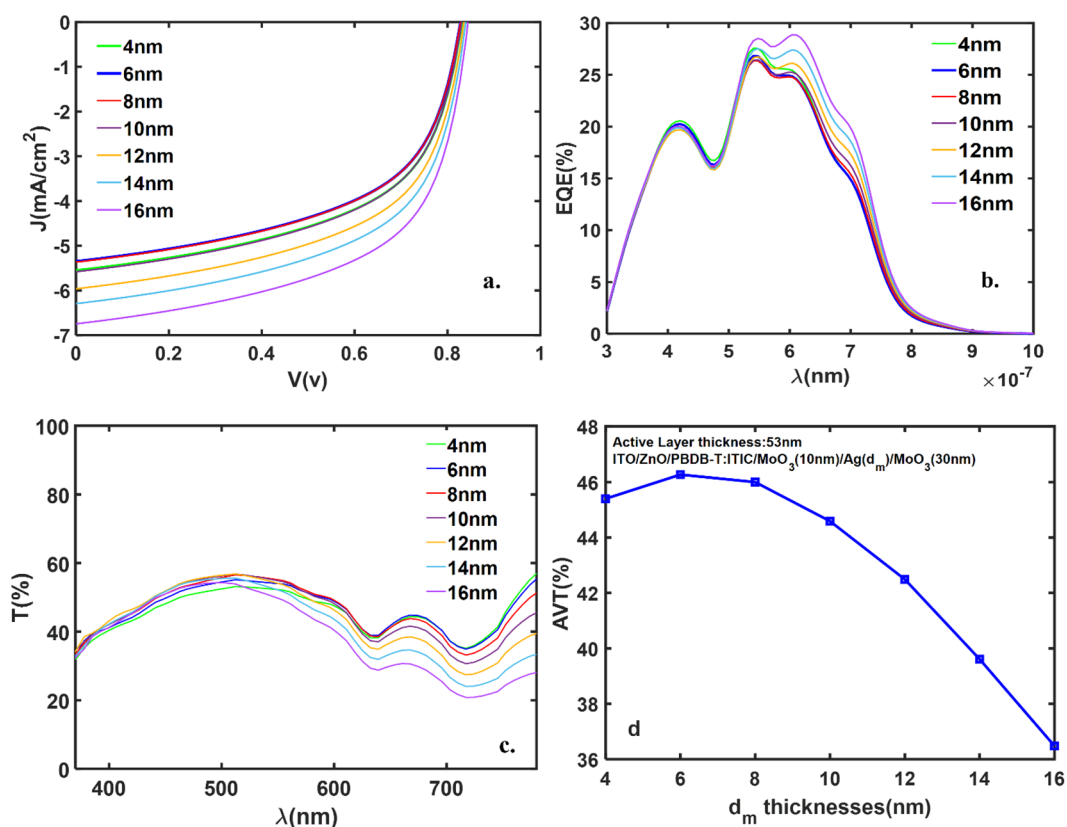
Figure 5. (**a**) The J-V curve, (**b**) the EQE as a function of wavelength, (**c**) T as a function of the wavelength, (**d**) the AVT as a function of d_m thicknesses for the devices with the active layer thickness of 53 nm.

mismatch between experimental and theoretical AVT with increasing the active layer thickness comes from the fitted absorption coefficient (Eq. 3) which has a very low deviation from experimental for thinner active layers.

It is well known that organic thin-film solar cells act as multilayer optical cavities in which the distribution of the optical field is governed by the effect of optical interference, due to the reflection of the incident light at the layer interfaces [41]. In the studied devices, the D/M/D top contact which includes 3 layers can be an important multi-layer for optical interference. On the other hand, as the model results for studied structures (Table. 2) are in very good agreement with the experimental data, so the model can be applied to the same structures with different Ag thicknesses in the D/M/D layers. For this purpose, all reported devices in Table 2 have been studied using different metal thicknesses in the D/M/D layer. The considered D/M/D layers has the thickness of MoO₃(10 nm)/Ag(dm)/MoO₃(30 nm) with d_m = 4, 6, 8, 10, 12, 14, 16 (nm). Using the theoretical model previously explained, all performance parameters such as the J-V curve, EQE, T, AVT, and color coordinates are calculated. As an example, for the devices with the active layer thickness of 53 nm, and d_m = 4, 6, 8, 10, 12, 14, 16 (nm), the performance parameters are presented in Fig. 5. As shown in Fig. 5a, with increasing the metal thickness, J_{SC} increases, but the V_{OC} does not change. In these devices, the exciton generation rate depends on the optical field intensity which is located close to the anode/active layer interface when light enters through

d_m (nm)	J_{SC} (mA/cm²)	FF(%)	V_{oc} (V)	PCE(%)	AVT(%)
4	5.55	55.49	0.82	3.27	45.40
6	5.35	54.66	0.82	3.11	46.27
8	5.36	54.60	0.82	3.10	46.00
10	5.58	55.28	0.82	3.28	44.59
12	6.70	57.86	0.84	4.19	42.49
14	5.96	55.68	0.84	3.59	39.61
16	6.74	57.98	0.84	4.22	36.48

Table 3. The calculated characteristic parameters of the ITO/ZnO/PBDB-T:ITIC/MoO$_3$/Ag/MoO$_3$ structures with D/M/D layers thickness of (10 nm/d_m/30 nm). The thickness of PBDB-T:ITIC active layer is fixed at 53 nm.

the D/M/D electrode under top illumination[42]. So, the metal thickness 'd_m' changes can dominantly affect the J_{SC} values. Figure 5b shows the EQE of the devices as a function of wavelengths, in which the highest EQE value belongs to thick metal layers, $d_m = 16$ nm. For all devices, the transmittance is higher than 25% for most visible wavelengths (Fig. 5c). Finally, Fig. 5d shows the AVT of the devices as a function of metal thickness. The AVT of all devices is higher than 36% and the maximum AVT is obtained for $d_m = 6$ nm. So, all devices can be used in the windows application.

All performance parameters for the device are presented in Table 3. As depicted in the table, all devices are practical for the window application with different PCE, while the highest value for PCE is for $d_m = 16$ nm. Also, the highest AVT was achieved for $d_m = 6$ nm, with 3.11% PCE.

In Fig. 6, we have presented the J-V curves of the devices with different active layer thicknesses and various d_m thicknesses. The figure shows that any change in d_m thickness doesn't change the V_{OC} values. The J_{SC} increases with increasing d_m and reaches 14.88 mA/cm² for the sample with an active layer thickness of $d_m = 16$ nm, where the fill factor is the lowest valve (46%-48%) in comparison with other samples. From the point of view of the fill factor, the sample with $d_m = 16$ nm and the active layer of 59 nm has the maximum FF, 70.49%.

In Fig. 7, the devices' J_{SC}, FF, and PCE are presented as a function of 'd_m' thickness and for various active layer thicknesses. As shown in the figure, for any fixed active layer thickness, with increasing 'd_m', the J_{SC} is increasing slightly, and the FF is almost constant, so, the PCE increases slightly. With increasing the thickness of active layers for any fixed 'd_m', the J_{SC} is increasing, and the FF hasn't any certain functionality, then, the PCE increases and reaches a maximum, decreases. The maximum value of PCE happens for samples with an active layer of about 100 nm. For devices with a thicker active layer (more than 100 nm), the FF was lower due to the increase in series resistance, which could be due to the distorted distribution of exciton generation within the active layer (most excitons are generated near the anode/active layer interface) and subsequent carrier transport towards respective electrodes.

To show the applicability of the studied devices in the windows application, the AVT values of the devices are shown in Fig. 8. By increasing the active layer thicknesses, the AVT is increasing, then decreases almost linearly. The maximum value for the AVT belongs to the ST-OSC with the active layer thicknesses of 59 nm (see Fig. 7c). As shown in the figure, for a fixed active layer thickness, the AVT value has a maximum at $d_m = 6$ nm, then with increasing the d_m value, the AVT decreases. The figure shows that all devices with different d_m and active layer thicknesses thicker than 114 nm deserve semitransparent solar cell conditions.

The CIE color space, including the coordinates of ST-OSC consisting of different active layer thicknesses and different 'd_m', is shown in Fig. 9. The color coordinates of translucent OSCs with an active layer thickness of about 90- 100 nm are located close to the color point or so-called "white dot" in the CIE chromaticity diagram. Proximity indicates that there is a good achromatic or neutral color sensations when looking through devices under AM1.5G illumination. Hence, these devices can transmit high-quality light with near white sensation to the human eye without changing the original color of an object. However, as the thickness of the active layer changes, the color coordinates move in different directions from the white dot. Also, the coordinates are sensitive to d_m values, and both coordinates x and y increase with increasing d_m (see the inset of Fig. 9). For a device with the best PCE and AVT, the thickness of the active layer is 100 nm and the color coordinates are slightly away from the achromatic point, however, the device does not alter the transmitted light by a large extent.

Conclusion

Semitransparent organic solar cells with an active layer of PBDB-T:ITIC and the top transparent electrode of D/M/D are studied. The effects of active layer thicknesses and metal (Ag) layer thickness in the top electrode on the solar cell performance are achieved. The results show that the devices with an active layer thickness of 100 nm have the highest PCE values regardless of any metal layer thickness in the D/M/D layers; the devices with an Ag layer thickness of 6 nm in D/M/D layers have the highest AVT values regardless any active layer thickness. The increasing metal layer thickness in D/M/D layers decreases the AVT and increases slightly the PCE values. For all devices with an active layer thickness thinner than 100 nm with any reported Ag layer thickness, AVT is higher than 25%, and the color coordinates of all these semi-transparent devices are close to the achromatic point. The devices with an active layer thickness of 53 nm and metal layer thickness of 6 nm, have AVT of more than 46%, and PCE of more than 3%.
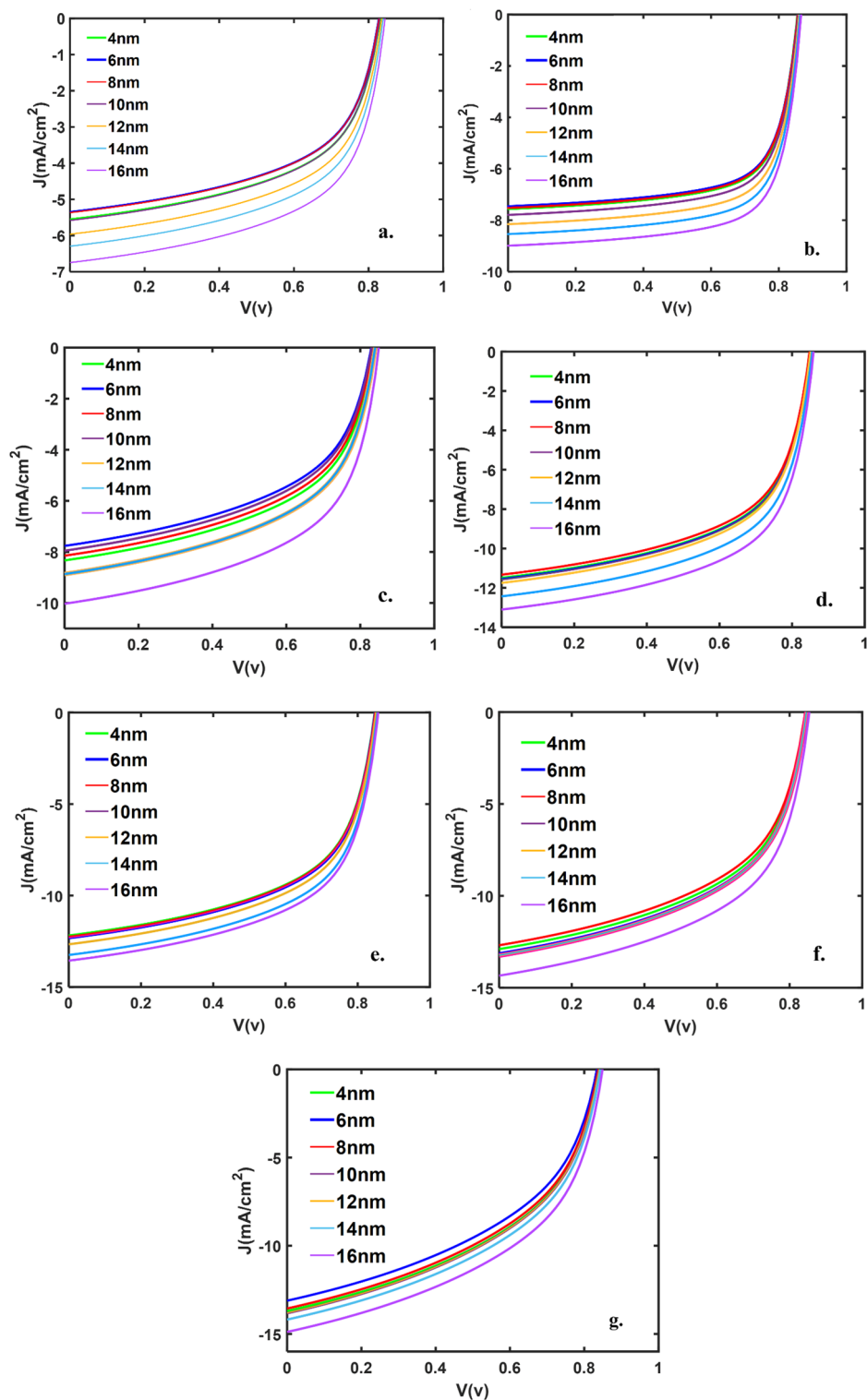
Figure 6. J-V curve for devices with a thickness of active layer (**a**) 53 nm, (**b**) 59 nm, (**c**) 72 nm, (**d**) 91 nm, (**e**) 100 nm, (**f**) 114 nm, (**g**) 143 nm, for various 'd$_m$' thicknesses.
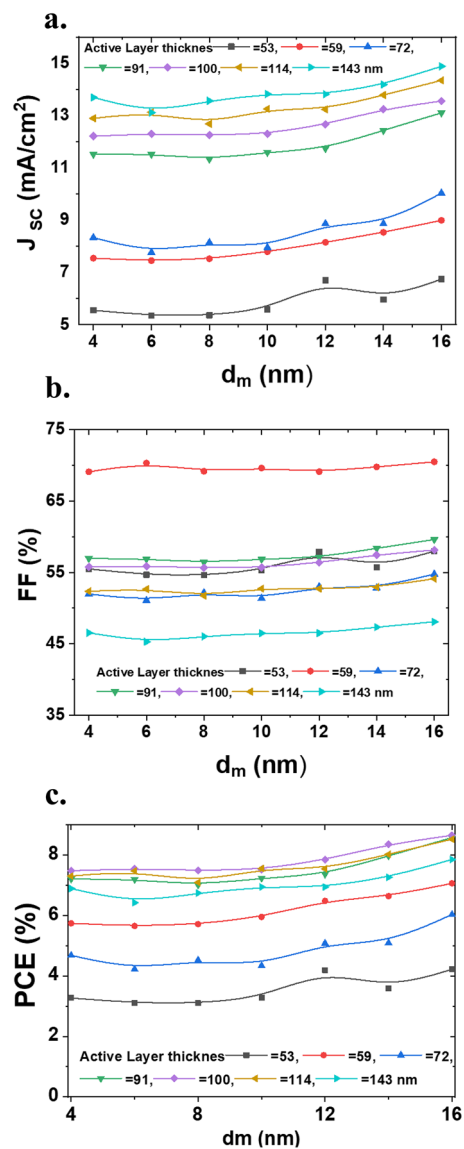
Figure 7. (**a**) The J_{SC}, (**b**) FF, and (**c**) PCE (%) of the devices as a function of active and 'd$_m$' layer thicknesses.
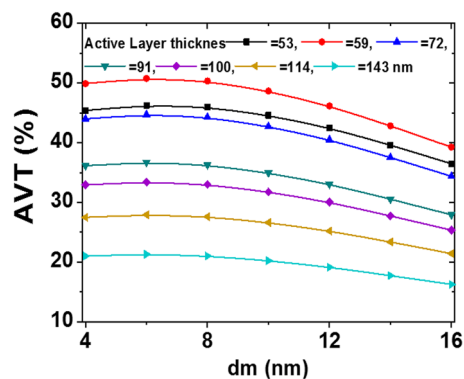
Figure 8. The AVT (%) of the devices as a function of active and 'd$_m$' layers thicknesses.
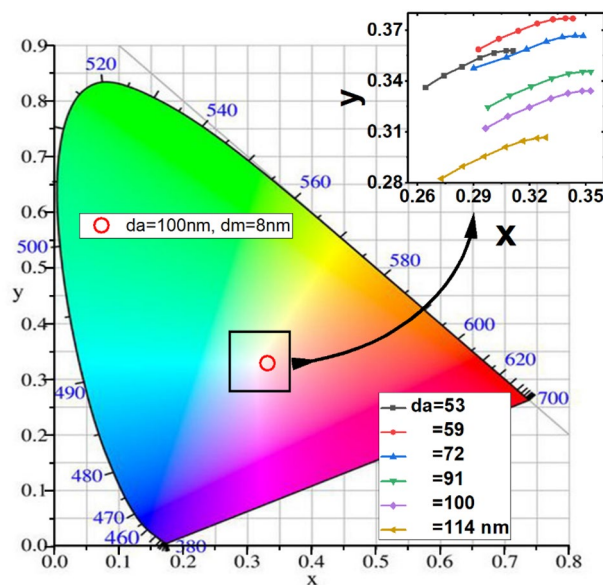
Figure 9. Representation of the color coordinate (x, y) of the ST-OSC with different active layers and d_m of D/M/D layer thicknesses, under standard D65 illumination light source on the CIE1931 color space.

Data availability

The datasets used and/or analysed during the current study available from the corresponding author on reasonable request.

References

1. Li, Y., Xu, G., Cui, C. & Li, Y. Flexible and semitransparent organic solar cells. *Adv. Energy Mater.* **8**(7), 1–28 (2018).
2. Schubert, M. B. & Werner, J. H. Flexible solar cells for clothing. *Mater. Today* **9**(6), 42–50 (2006).
3. Lunt, R. R. Theoretical limits for visibly transparent photovoltaics. *Appl. Phys. Lett.* **101**(4), 043902 (2012).
4. Schopp, N., Brus, V. V. & Nguyen, T. Q. On optoelectronic processes in organic solar cells: From opaque to transparent. *Adv. Opt. Mater.* **9**(3), 1–9 (2021).
5. Xu, C. *et al.* Wide bandgap polymer with narrow photon harvesting in visible light range enables efficient semitransparent organic photovoltaics. *Adv. Funct. Mater.* **31**(52), 1–8 (2021).
6. Schopp, N., Brus, V. V., Lee, J., Bazan, G. C. & Nguyen, T. Q. A simple approach for unraveling optoelectronic processes in organic solar cells under short-circuit conditions. *Adv. Energy Mater.* **11**(1), 1–10 (2021).
7. Ray, P. Renewable energy and sustainability. *Clean Technol. Environ. Policy* **21**(8), 1517–1533 (2019).
8. Zhao, F. *et al.* Single-junction binary-blend nonfullerene polymer solar cells with 12.1% efficiency. *Adv. Mater.* **29**(18), 1–7 (2017).
9. Upama, M. B. *et al.* High performance semitransparent organic solar cells with 5% PCE using non-patterned MoO₃/Ag/MoO₃ anode. *Curr. Appl. Phys.* **17**(2), 298–305 (2017).
10. Upama, M. B. *et al.* Optical modelling of P3HT: PC71BM semi-transparent organic solar cell. *Opt. Quantum Electron.* **49**(1), 1–6 (2017).
11. Schopp, N., Nguyen, T. Q. & Brus, V. V. Optical expediency of back electrode materials for organic near-infrared photodiodes. *ACS Appl. Mater. Interfaces* **13**(23), 27217–27226 (2021).
12. Jeon, I. *et al.* Metal-electrode-free window-like organic solar cells with p-doped carbon nanotube thin-film electrodes. *Sci. Rep.* **6**, 1–2 (2016).
13. Liu, Z. *et al.* The application of highly doped single-layer graphene as the top electrodes of semitransparent organic solar cells. *ACS Nano* **6**(1), 810–818 (2012).
14. Shi, Y. *et al.* Work function engineering of graphene electrode via chemical doping. *ACS Nano* **4**(5), 2689–2694 (2010).
15. Xu, G. *et al.* High-performance colorful semitransparent polymer solar cells with ultrathin hybrid-metal electrodes and fine-tuned dielectric mirrors. *Adv. Funct. Mater.* **27**(15), 1–10 (2017).
16. Yu, W. *et al.* Semitransparent polymer solar cells with simultaneously improved efficiency and color rendering index. *Phys. Chem. Chem. Phys.* **17**(37), 23732–23740 (2015).
17. Chen, K. S. *et al.* Semi-transparent polymer solar cells with 6% PCE, 25% average visible transmittance and a color rendering index close to 100 for power generating window applications. *Energy Environ. Sci.* **5**(11), 9551–9557 (2012).
18. Yu, W. *et al.* Highly efficient semitransparent polymer solar cells with color rendering index approaching 100 using one-dimensional photonic crystal. *ACS Appl. Mater. Interfaces* **7**(18), 9920–9928 (2015).
19. Zheng, Z. *et al.* Efficient charge transfer and fine-tuned energy level alignment in a THF-processed fullerene-free organic solar cell with 11.3% efficiency. *Adv. Mater.* **29**(5), 3–8 (2017).
20. Huang, J. *et al.* Highly efficient organic solar cells consisting of double bulk heterojunction layers. *Adv. Mater.* **29**(19), 1606729 (2017).
21. Yao, H. *et al.* Achieving highly efficient nonfullerene organic solar cells with improved intermolecular interaction and open-circuit voltage. *Adv. Mater.* **29**(21), 1–8 (2017).
22. Chen, S. *et al.* An all-solution processed recombination layer with mild post-treatment enabling efficient homo-tandem nonfullerene organic solar cells. *Adv. Mater.* **29**(6), 1–7 (2017).

23. Schopp, N. *et al.* Understanding interfacial recombination processes in narrow-band-gap organic solar cells. *ACS Energy Lett.* **7**(5), 1626–1634 (2022).
24. Zhang, Y. *et al.* Nonfullerene polymer solar cells based on a perylene monoimide acceptor with a high open-circuit voltage of 1.3 V. *Adv. Funct. Mater.* **27**(10), 1603892 (2017).
25. Gupta, V., Bagui, A. & Singh, S. P. molecular engineering of highly efficient small molecule nonfullerene acceptor for organic solar cells. *Adv. Funct. Mater.* **27**(2), 1603820 (2017).
26. Qin, Y. *et al.* Highly efficient fullerene-free polymer solar cells fabricated with polythiophene derivative. *Adv. Mater.* **28**(42), 9416–9422 (2016).
27. Li, S. *et al.* Energy-level modulation of small-molecule electron acceptors to achieve over 12% efficiency in polymer solar cells. *Adv. Mater.* **28**(42), 9423–9429 (2016).
28. Holliday, S. *et al.* High-efficiency and air-stable P3HT-based polymer solar cells with a new non-fullerene acceptor. *Nat. Commun.* **7**, 1–11 (2016).
29. Zhao, W. *et al.* Fullerene-free polymer solar cells with over 11% efficiency and excellent thermal stability. *Adv. Mater.* **28**(23), 4734–4739 (2016).
30. Min, Y., Huh, J. & Ho, W. Optimization of thickness and morphology of active layer for high performance of bulk-heterojunction organic solar cells. *Solar Energy Mater Solar Cells* **94**, 1118–1124 (2010).
31. Upama, M. B. *et al.* High-efficiency semitransparent organic solar cells with non-fullerene acceptor for window application. *ACS Photonics* **4**(9), 2327–2334 (2017).
32. Cheyns, D. *et al.* Analytical model for the open-circuit voltage and its associated resistance in organic planar heterojunction solar cells. *Phys. Rev. B* **77**(16), 165332 (2008).
33. Piralaee, M. & Asgari, A. Bimetallic core–shell nanoparticles to improve the absorption of P3HT: PCBM organic solar cell. *Appl. Opt.* **60**(29), 9087 (2021).
34. Mackay, T. G. & Lakhtakia, A. The transfer-matrix method in electromagnetics and optics. *Synth. Lect. Electromagn.* **1**(1), 1–126 (2020).
35. Çetinkaya, Ç. *et al.* Design and fabrication of a semi-transparent solar cell considering the effect of the layer thickness of MoO3/Ag/MoO3 transparent top contact on optical and electrical properties. *Sci. Rep.* **11**(1), 1–18 (2021).
36. Hu, Z. *et al.* A critical review on semitransparent organic solar cells". *Nano Energy* **78**, 105376 (2020).
37. Brus, V. V. *et al.* Solution-processed semitransparent organic photovoltaics: From molecular design to device performance. *Adv. Mater.* **31**(30), 1–26 (2019).
38. Yang, C., Liu, D., Bates, M., Barr, M. C. & Lunt, R. R. How to accurately report transparent solar cells. *Joule* **3**(8), 1803–1809 (2019).
39. Ma, X. *et al.* Layered optimization strategy enables over 17.8% efficiency of layer-by-layer organic photovoltaics. *Chem. Eng. J.* **442**(P2), 136368 (2022).
40. Xu, W. *et al.* Achieving 17.5% efficiency for polymer solar cells via a donor and acceptor layered optimization strategy. *J. Mater. Chem. C* **10**(14), 5489–5496 (2022).
41. Ham, J., Kim, S., Jung, G. H., Dong, W. J. & Lee, J. L. Design of broadband transparent electrodes for flexible organic solar cells. *J. Mater. Chem. A* **1**(9), 3076–3082 (2013).
42. Joseph, B., Pogrebnaya, T. & Kichonge, B. Semitransparent building-integrated photovoltaic: Review on energy performance, challenges, and future potential. *Int. J. Photoenergy* **2019**, 1–17 (2019).

Author contributions

All authors have the same contributions to the work and the manuscript preparation.

Competing interests

The authors declare no competing interests.

Additional information